Instability of shielded surface temperature vortices

Benjamin J. Harvey * and Maarten H. P. Ambaum

Department of Meteorology, University of Reading, Reading, UK

Xavier J. Carton

LPO, UBO/UEB, Brest, France

* *Corresponding author address:* Ben Harvey, Department of Meteorology, University of Reading, PO Box 243, Reading, RG6 6BB, United Kingdom

E-mail: b.j.harvey@reading.ac.uk

ABSTRACT

The stability characteristics of the surface quasi-geostrophic shielded Rankine vortex are found using a linearised contour dynamics model. We analyse both the normal modes and non-modal evolution of the system and compare the results to two previous studies. One is a numerical study of the instability of smooth surface quasi-geostrophic vortices with which we find qualitative similarities and the other is a corresponding study for the two-dimensional Euler system with which we highlight several notable differences.

1. Introduction

The surface quasi-geostrophic (SQG) model (Held et al. 1995) is an approximation to the motion of a rapidly rotating stratified fluid near a horizontal boundary. It represents planar advection of the boundary temperature field under the assumption of zero interior potential vorticity. This is in essence a two dimensional system whereby the streamfunction is determined entirely by the boundary temperature field via a Green's function proportional to $1/r$. Applications of the model include the evolution of tropopause undulations (Juckes (1994), Juckes (1995), Muraki and Snyder (2007)) and near-surface oceanic vortices (Lapeyre and Klein 2006). This type of dynamics has also been studied by Blumen (1978) under the name of uniform potential vorticity flow.

Carton (2009) (hereafter C09) provides a numerical study of smooth shielded vortices in the SQG model and compares the evolutions with those of unstable vortices under the more familiar two-dimensional Euler dynamics. Here the complementary analytic study is presented in which linear growth rates of perturbations are calculated for a simple class

of shielded SQG vortex, the shielded surface Rankine vortex. By this we mean the SQG analogue of the usual shielded Rankine vortex of two-dimensional Euler dynamics: an inner circle of temperature $\theta = \theta_0$ surrounded by an outer annulus of temperature $\theta = \theta_1$. In the following we use the same notation and conventions as C09 which should also be referred to for a full description of the model and its applications.

The shielded surface Rankine vortex provides the simplest analytically tractable example of an unstable SQG vortex. Further, the corresponding two-dimensional Euler problem is well studied (Flierl 1988) so this set-up provides a fruitful source of comparisons between the two systems. The analytical treatment has become possible since Harvey and Ambaum (2010b) derived the dispersion relation for a single-step surface Rankine vortex, that is, a circular patch of uniform temperature anomaly analogous to the Rankine vortex of two-dimensional Euler dynamics. We review the methodology and the main results we require from this study in Section 2 and then analyse the shielded problem in Section 3. A comparison is made with the results of C09 in Section 4 and conclusions are provided in Section 5.

2. Single-step surface Rankine vortex dispersion relation

The dispersion relation for linear perturbations to a single-step surface Rankine vortex, or temperature 'patch', of the form

$$\bar{\theta}(r) = \begin{cases} \theta_0 & r < a \\ 0 & r > a, \end{cases} \tag{1}$$

where a is the patch radius and θ_0 the temperature anomaly of the vortex, is derived in Harvey and Ambaum (2010b). Here we review the methodology and the main results from that study. It is shown there that the azimuthal velocity field corresponding to (1) can be written as

$$\bar{u}(r) = \theta_0 \mathrm{E}_1(r/a) \tag{2}$$

where we introduce the notation

$$\mathrm{E}_n(r/a) \equiv \int_0^\infty \mathrm{J}_n(\kappa)\mathrm{J}_n(\kappa r/a)\,\mathrm{d}\kappa, \tag{3}$$

with J_n the Bessel functions of the first kind. Figure 1(a) illustrates (1) and (2) graphically. Note the logarithmic singularity in $\bar{u}$ at $r = a$ which we discuss below.

The dispersion relation is derived by perturbing the patch boundary to the new position

$$r = a(1 + \mathrm{Re}(\eta(t)e^{in\varphi})), \tag{4}$$

where φ is the azimuthal coordinate, and linearising the equation for material advection of the boundary for small η. The linearised equation of motion is

$$\frac{\mathrm{d}\eta}{\mathrm{d}t} = \lim_{r\to a}\left(-\frac{in}{r}\bar{u}\eta + \frac{1}{a}v'e^{-in\varphi}\right), \tag{5}$$

where $v'(r, \varphi, t)$, the linearised perturbation radial velocity field, is derived in Harvey and Ambaum (2010b) as

$$v' = \frac{in}{r}a\eta\theta_0\mathrm{E}_n(r/a)e^{in\varphi}. \tag{6}$$

Note that the right hand side of (5) is the sum of the azimuthal advection of the perturbation by the basic state (first term) and the radial advection of the basic state by the perturbation (second term). Both of these terms are singular at $r = a$, but the combination (5) is

regular. The velocity singularity is a generic feature of temperature discontinuities under SQG inversion. However, the singular component of the velocity is always aligned along the discontinuity and the normal component remains finite. Therefore the evolution of the temperature field remains relatively slow (Held et al. 1995). This alignment is apparent here through the cancellation of the singularities in (5), as discussed by Harvey and Ambaum (2010b). The justification for using this basic state, despite the qualitative difference with the smooth profiles of C09, comes from the fact that wave propagation on a slightly smoothed discontinuity is regular in the sharp edge limit, as shown by Juckes (1995).

Putting $\eta(t) \propto e^{-i\omega_n t}$ and substituting for $\bar{u}$ and v' from (2) and (6) in (5) gives the dispersion relation we are after:

$$\omega_n = \frac{\theta_0 n}{a} \lim_{r\to a}(\mathrm{E}_1(r/a) - \mathrm{E}_n(r/a)), \tag{7}$$

which is evaluated analytically in Harvey and Ambaum (2010b) as

$$\omega_n = \frac{\theta_0 n}{a}\frac{1}{\pi}\sum_{j=2}^{n}\left(\frac{1}{j-1/2}\right) \equiv \frac{\theta_0 n}{a}\alpha_n. \tag{8}$$

We note that the two-dimensional Euler dispersion relation for waves on a vortex patch can be obtained similarly. The less localised Green's function, proportional to $\log r$ in that case, introduces a factor k^{-1} into the integrand of (3) and the integral can then be evaluated as $\mathrm{E}_n^{\mathrm{2DE}}(1) = a/2n$ (Gradshteyn and Ryzhic 2000) so (7) reduces to the standard result

$$\omega_n^{\mathrm{2DE}} = \frac{q_0}{2}(n-1), \tag{9}$$

where q_0 is the vorticity value of the patch. An important difference between (9) and (8) is the a in the prefactor: the phase speeds of perturbations, $c_\mathrm{p} = \omega a/n$, on the SQG vortex are independent of the vortex radius. This is to be expected on dimensional grounds since

θ has the dimension of a velocity field whereas the vorticity, q, in the two-dimensional Euler system has the dimension of a frequency.

3. Shielded surface Rankine vortex dispersion relation

We now use the method from Section 2 to find analytic expressions for the linear growth rates of perturbations on a shielded surface Rankine vortex. We write the basic state as

$$\bar{\theta}(r) = \begin{cases} \theta_0 & r < a \\ \theta_1 & a < r < b \\ 0 & r > b, \end{cases} \tag{10}$$

with $a < b$ the radii of the temperature jumps and θ_0, θ_1 the inner and outer temperature anomalies respectively. Through linearity and (2) the corresponding basic state velocity field is

$$\bar{u}(r) = (\theta_0 - \theta_1)\mathrm{E}_1(r/a) + \theta_1 \mathrm{E}_1(r/b), \tag{11}$$

an example of which is illustrated, along with the profile (10), in Figure 1(b).

To analyse the evolution of perturbations on this basic state we follow the procedure from Section 2 except that here there are two boundaries which must be taken into account. Consider perturbing each boundary independently to the new positions

$$r = r_1(\varphi, t) \equiv a(1 + \mathrm{Re}(\eta(t)e^{in\varphi})) \quad \text{and} \quad r = r_2(\varphi, t) \equiv b(1 + \mathrm{Re}(\nu(t)e^{in\varphi})), \tag{12}$$

and linearising the equation for material advection of each boundary, for small η and ν. The

result is a pair of equations analogous to (5),

$$\frac{\mathrm{d}\eta}{\mathrm{d}t} = \lim_{r\to a}\left(-\tfrac{in}{r}\bar{u}\eta + \tfrac{1}{a}v'e^{-in\varphi}\right) \tag{13}$$

$$\frac{\mathrm{d}\nu}{\mathrm{d}t} = \lim_{r\to b}\left(-\tfrac{in}{r}\bar{u}\nu + \tfrac{1}{b}v'e^{-in\varphi}\right), \tag{14}$$

where $\bar{u}(r)$ is given by (11) and the linearised perturbation radial velocity $v'(r,\varphi,t)$ is likewise a linear sum of contributions from each boundary of the form (6):

$$v' = \frac{in}{r}(a\eta(\theta_0-\theta_1)\mathrm{E}_n(r/a) + b\nu\theta_1\mathrm{E}_n(r/b))e^{in\varphi}. \tag{15}$$

We now substitute for $\bar{u}$ and v', from (11) and (15) into (13) and (14), and write the system in matrix form for convenience. First we define the nondimensional parameters

$$\lambda = b/a \quad \text{and} \quad \mu = \theta_1/\theta_0 \tag{16}$$

to simplify notation, and note from (3) that $\mathrm{E}_n(1/\lambda) = \lambda\mathrm{E}_n(\lambda)$. The system (13)-(14) can then be written

$$i\frac{\mathrm{d}}{\mathrm{d}t}\begin{pmatrix}\eta\\ \nu\end{pmatrix} = \frac{\theta_0 n}{a}\begin{pmatrix}(1-\mu)\alpha_n + \lambda\mu\mathrm{E}_1(\lambda) & -\lambda^2\mu\mathrm{E}_n(\lambda)\\ -\dfrac{(1-\mu)\mathrm{E}_n(\lambda)}{\lambda^2} & \dfrac{\mu\alpha_n}{\lambda} + \frac{(1-\mu)\mathrm{E}_1(\lambda)}{\lambda}\end{pmatrix}\begin{pmatrix}\eta\\ \nu\end{pmatrix} \tag{17}$$

$$\equiv \mathbf{F}\begin{pmatrix}\eta\\ \nu\end{pmatrix}, \tag{18}$$

where α_n is defined in (8). The matrix $\mathbf{F}$ contains all the information for the evolution of linear perturbations. The diagonal elements represent the propagation of the disturbances on each boundary whereas the off-diagonal elements represent the interaction between the boundaries. Here we have chosen θ_0/a as the dimensional frequency scale for consistency with the study of Flierl (1988). That is, we imagine a central vortex of amplitude θ_0 and

radius a and ask how the different 'shields' modify the vortex behaviour. An alternative, which we discuss further below, is to focus on the filament-like nature of the instability. That is, consider the outer annulus as a circular filament of width $b-a$, the instability of which is modified by the circular geometry and the presence of the central vortex.

The normal mode frequencies of the system are given by the eigenvalues of $\mathbf{F}$ which take the form

$$\Omega_n^{\pm} = \frac{\mathrm{tr}(\mathbf{F})}{2} \pm \sqrt{\left(\frac{\mathrm{tr}(\mathbf{F})}{2}\right)^2 - \det(\mathbf{F})}. \tag{19}$$

There are therefore unstable normal modes when $\mathrm{tr}(\mathbf{F})^2 < 4\det(\mathbf{F})$. This boundary of stability in (λ, μ)-space is shown in Figure 2(a) for several wavenumbers. To interpret the figure we note that the SQG analogue of the Rayleigh theorem requires a radial temperature profile to contain regions of opposing gradient for growing normal modes to exist (see C09). These are only present in (10) if $\mu > 1$ or $\mu < 0$ and the regions of normal mode growth in Figure 2(a) are indeed contained within these regions.

Figure 2(b) shows the corresponding two-dimensional Euler calculation for comparison, following Figure 2 of Flierl (1988). That is, the stability boundaries for a shielded Rankine vortex consisting of an inner circular patch with vorticity q_0 and an outer annulus with vorticity q_1. The two plots have many qualitative similarities, the main difference being that the $n = 2$ mode is stable for all $q = q_1/q_0 > 0$ in the two-dimensional Euler case whereas for the SQG system there is a region of parameter space with $\mu > 0$ where the $n = 2$ mode is unstable. Another difference is that for the SQG case the boundaries of stability do not all continue to large λ. For the two-dimensional Euler case the boundaries of stability all tend towards $q = (n-1)/(n-2)$ at large λ (see Flierl (1988)) whereas for the SQG system

modes $n = 2 - 4$ satisfy

$$\mu \sim 1 + \left(\frac{1}{2\alpha_n} - 1\right)\frac{1}{\lambda} \quad \text{for} \quad \lambda \gg 1, \tag{20}$$

but modes with $n \geq 5$ (for which $\alpha_n > 1/2$) are stable for all μ at λ larger than a critical value given by the solution to $\lambda_c^2 \mathrm{E}_1(\lambda_c) = \alpha_n$. This expression is found by noting that the stability boundary is given by the implicit equation $\mathrm{tr}(\mathbf{F})^2 = 4\det(\mathbf{F})$. Expanding this equation for $\lambda \gg 0$ we find the expression (20), where we have also used the asymptotic result derived in Harvey and Ambaum (2010b) that $\mathrm{E}_n \sim C_n/\lambda^{n+1}$ with $C_1 = 1/2$.

The normal modes of (19) are special perturbation configurations which preserve their shape in time. In general, unstable solutions to (18) undergo an initial period of transient development during which they align towards the growing normal mode shape (see Farrell and Ioannou (1996) and Carton et al. (2010) for further discussion). To analyse this non-modal evolution we write the full solution of (18) as

$$\boldsymbol{\eta}(t) = \mathbf{M}(t)\boldsymbol{\eta}(0), \tag{21}$$

where $\boldsymbol{\eta} = (\eta, \nu)^{\mathrm{T}}$ and the matrix $\mathbf{M}$ is formed from the eigenvectors $\mathbf{f}_+$ and $\mathbf{f}_-$ of $\mathbf{F}$ (corresponding to Ω_n^+ and Ω_n^- respectively):

$$\mathbf{M} = (\mathbf{f}_+, \mathbf{f}_-) \begin{pmatrix} e^{-\mathrm{i}\Omega_n^+ t} & 0 \\ 0 & e^{-\mathrm{i}\Omega_n^- t} \end{pmatrix} (\mathbf{f}_+, \mathbf{f}_-)^{-1}, \tag{22}$$

and measure disturbance size using the r.m.s waveslope norm

$$N(t) = \left(\frac{1}{2\pi}\int_0^{2\pi}\left[\left(\frac{1}{a}\frac{\partial r_1}{\partial \varphi}\right)^2 + \left(\frac{1}{b}\frac{\partial r_2}{\partial \varphi}\right)^2\right] d\varphi\right)^{1/2} = \frac{n}{\sqrt{2}}|\boldsymbol{\eta}(t)| \tag{23}$$

which is representative of the size of some of the nonlinear terms in the full evolution equations and is therefore a diagnostic for nonlinear development (Dritschel 1989). The maximum

value of the norm at any given time, the so-called singular mode amplitude, then takes the value

$$N_{\rm s}(t) \equiv \max_{\boldsymbol{\eta}(0)} (N(t)) = \frac{n}{\sqrt{2}} \max_{\boldsymbol{\eta}(0)} \left(\sqrt{\boldsymbol{\eta}^*(0) \mathbf{M}^* \mathbf{M} \boldsymbol{\eta}(0)} \right) \quad (24)$$

$$= N(0) \sqrt{\text{largest eigenvalue of } \mathbf{M}^* \mathbf{M}}, \quad (25)$$

where * represents the conjugate transpose. It can be shown that (Farrell and Ioannou 1996) $N_{\rm s}$ has the following asymptotic limit for small times ($t \ll |\Omega_n^{\pm}|^{-1}$)

$$N_{\rm s}(t) \sim N(0)(1 + \frac{|F_{12} - F_{21}|}{2} t), \quad (26)$$

where F_{12} and F_{21} are the off-diagonal elements of $\mathbf{F}$, and for large times ($t \gg |\Omega_n^{\pm}|^{-1}$)

$$N_{\rm s}(t) \sim N(0) \frac{|F_{12} - F_{21}|}{2 {\rm Im}(\Omega_n^+)} e^{{\rm Im}(\Omega_n^+) t}, \quad (27)$$

if ${\rm Im}(\Omega_n^+) > 0$ and $N_{\rm s}(t) \sim 0$ otherwise. For small times, $N_{\rm s}$ grows linearly at a rate larger than the normal mode rate, whereas at large times the growth is exponential at the normal mode rate. The non-modal evolution is only short lived, but it has a long lived effect in that the absolute amplitude of disturbances can be larger than the corresponding normal mode by the factor $|F_{12} - F_{21}|/2{\rm Im}(\Omega_n^+)$. This factor varies over parameter space and asymptotes towards infinity at the stability boundaries where ${\rm Im}(\Omega_n^+) \to 0$.

Figure 3 shows values of the corresponding singular mode equivalent growth rate,

$$\sigma_{\rm s}(t) = \frac{\log(N_{\rm s}(t)/N(0))}{t}, \quad (28)$$

to illustrate the non-modal evolution. The times shown are $t \to 0$ (given by (26)) and $t \to \infty$ (given by (27)), and two intermediate cases, $t = 4a/\theta_0$ and $t = 16a/\theta_0$. The figure is consistent with the notion that non-modal disturbances of wavenumbers within the

range of growing normal modes undergo a transient period of growth potentially larger than the corresponding normal mode growth rate during which they adjust towards the normal mode shape, followed by what is effectively normal mode growth. Non-modal disturbances outside the range of the growing normal modes continually undulate around their initial configuration resulting in a σ_s which decays in time. The ridges, particularly apparent in panel (c), are a result of this undulatory non-modal behaviour.

4. Completely shielded vortices

Returning now to analyse the normal modes in more detail, we focus on vortices with zero net integrated temperature anomaly, that is,

$$(\lambda^2 - 1)\mu = -1, \tag{29}$$

which is illustrated in Figure 2(a) by the solid line. This class of vortices is important because it represents vortices with a more localised influence than not-completely-shielded cases. In particular, the class of vortices studied by C09 are completely shielded.

Figure 4(a) shows the normal mode growth rates of perturbations for completely shielded vortices as a function of λ. The SQG vortices display the familiar behaviour also observed in the two-dimensional Euler case, through theory and experiment, that the wavenumber of the fastest growing normal mode is dependent on the vortex profile, with progressively higher modes being relevant for smaller λ, or larger μ. The increase in growth rate as $\lambda \to 1$ is consistent with a consideration of filament instability, as we show below. First we compare the growth rates to those of the C09 study.

The family of vortices studied by C09 have temperature profiles of the form

$$\bar{\theta}(r) = \Theta(r) \equiv \Theta_0(\alpha) \left(1 - \frac{\alpha}{2}\left(\frac{r}{R}\right)^{\alpha}\right) e^{-(r/R)^{\alpha}} \tag{30}$$

where r is the radial coordinate, R and α are positive constants and $\Theta_0(\alpha)$ is a normalisation factor such that the corresponding azimuthal velocity field $\bar{u}(r)$ satisfies $\max(\bar{u}) = u_0$. These profiles consist of a central temperature maximum surrounded by an annulus of negative temperature anomaly, as illustrated in Figure 5. We approximate them as shielded surface Rankine vortices by choosing suitable values for θ_0, θ_1 and the sizes of the inner and outer regions.

There is freedom in choosing these parameters; we choose them to satisfy the following four constraints:

$$r = a \qquad \text{minimises} \quad \mathrm{d}\Theta/\mathrm{d}r \tag{31}$$

$$r = b \qquad \text{maximises} \quad \mathrm{d}\Theta/\mathrm{d}r \tag{32}$$

$$\int_0^{\infty} \bar{\theta}(r) r \, \mathrm{d}r = 0 \tag{33}$$

$$\int_0^{a} \bar{\theta}(r) r \, \mathrm{d}r = \int_0^{a} \Theta(r) r \, \mathrm{d}r. \tag{34}$$

That is, the locations of the jumps coincide with the points of steepest temperature gradient and the two temperature values θ_0 and θ_1 are chosen so that both the total integrated temperature anomaly is zero and the integrated temperature anomaly in the range $r < a$ equals that of the smooth profiles. The choice is of course not unique, but it suffices to provide a qualitative comparison between the systems. Figure 5 illustrates this choice of parameters for several values of α. The differences between the two growth rates is expected

to be sensitive in particular for small α where the smooth profiles differ most from the Rankine profiles.

The vortex parameters satisfying the constraints (31)-(34) are given by

$$\begin{pmatrix} a \\ \\ b \end{pmatrix} = R \left[\frac{3\alpha+1}{2\alpha} \mp \sqrt{\left(\frac{3\alpha+1}{2\alpha}\right)^2 - \frac{(\alpha+2)(\alpha-1)}{\alpha^2}} \right]^{1/\alpha}, \tag{35}$$

$$\theta_0 = \Theta_0(\alpha) e^{-(a/R)^\alpha}, \quad \theta_1 = \frac{-\theta_0 a^2}{b^2 - a^2} \tag{36}$$

where Θ_0 and α are as in (30). Figure 4(b) shows the corresponding normal mode growth rates, $\mathrm{Im}(\Omega_n)$, as a function of α. Note that the data plotted here is identical to that of Figure 4(a) except for the choice of scalings.

Also shown in Figure 4(b) are the numerically obtained growth rates from C09 for the corresponding smooth cases. There is a clear similarity between the two cases. The main difference is a shift towards higher α values in our figure since the first unstable mode appears near $\alpha = 3$ whereas there are unstable modes from $\alpha = 2$ in C09. The magnitude of the growth rates, however, are comparable between the two cases.

As mentioned above, the increase in growth rates for λ close to one, or equivalently large α, is consistent with the nature of filament instability in SQG dynamics. For comparison, a straight temperature filament of width L with a 'top-hat' profile, analogous to the Rayleigh problem of two-dimensional Euler dynamics, is unstable with normal mode growth rates given by

$$\sigma_{\mathrm{fil}} = \frac{\theta}{L} \mathrm{F}(\kappa) \tag{37}$$

where F is a function of the non-dimensional wavenumber $\kappa = kL$ (Juckes (1995); Harvey

and Ambaum (2010a)). As such, we define a scaling factor

$$S \equiv \frac{\sqrt{|\theta_1(\theta_0 - \theta_1)|}}{b-a} = \frac{\theta_0}{a}\frac{\lambda}{(\lambda+1)(\lambda-1)^2} \tag{38}$$

which is the ratio of a temperature scale (the geometric mean of the two temperature jumps) and the annulus width. Figure 6(a) shows that for unstable SQG vortices satisfying (29), the maximum growth rate is always remarkably close to $\max(\mathrm{F})S \approx 0.1292S$. We expect a similar result to hold for the two dimensional Euler system, except in that case there is no length scale so the instability growth rates will just be proportional to the geometric mean of the two vorticity jumps.

To highlight the link to the filament instability further, Figure 6(b) shows the dispersion relation calculated for several vortices towards the limit of a large, but weak, central vortex with an outer annulus of fixed width L, i.e. $\lambda \to 1$ with $b - a = L$. The wavenumber n is scaled to coincide with the wavenumber κ of the filament in this limit,

$$\kappa_{\mathrm{equiv}} = \frac{n}{a}(b-a) = n(\lambda - 1), \tag{39}$$

and the growth rates are again scaled by S of equation (38). The growth rates do indeed appear to coincide with those of the straight filament in the limit of $\lambda \to 1$. The correction for larger λ shifts the growth rate curve to slightly larger κ_{equiv} values on average but, consistent with the discussion above, does not alter the maximum growth rate by very much. This shift in the maximum growth rate seems to be purely a geometric effect of the curvature.

5. Discussion and Conclusions

The linear stability of the SQG shielded Rankine vortex has been investigated analytically. The study explains the numerical results obtained by C09 for a class of similar, but smooth, temperature profiles as well as providing a comparison to the well-studied two-dimensional Euler case.

The instability is shown to be related to filament instability in the relevant limit and is remarkably similar even far from this limiting case. The interesting differences to the two-dimensional Euler case are a result of the scaling between the advected quantity and the flow field, which is apparent in the growth rate of the filament instability. Harvey and Ambaum (2010a) discuss this further in the context of a filament under strain and shear.

As a check of the theory, nonlinear simulations of the completely shielded vortices have been run at high resolution with a pseudo-spectral code. This was achieved by (very) slightly smoothing the vortex profile discontinuities. The experiments showed vortex breaking on the linearly most unstable mode within a shift towards larger λ of order 0.05. In a similar fashion to the corresponding two-dimensional Euler case of Morel and Carton (1994), the numerical experiments did not evidence nonlinear stabilisation into multipoles. Instead the outer annulus breaks nonlinearly into smaller vortices which then pull the central vortex apart and disperse as dipoles. However, as in the two-dimensional Euler case, stable multipoles can be achieved if an annulus of zero temperature is introduced between the core vortex and the active periphery.

An interesting problem following on from this study is to investigate the corresponding baroclinic problem, that is, to consider two vertically separated SQG temperature patches

of opposite sign. This can be done either in an unbounded fluid, as an approximation to an oceanic heton, or confined by horizontal boundaries, as a model of atmospheric baroclinic instability on the hemispheric scale. This would put the model of Eady (1949) into a more realistic setting. A similar framework could be applied in either case.

Finally, we conclude by noting that this study provides further evidence towards considering the often overlooked SQG model, in addition to the two-dimensional Euler system, as an important model of geophysical processes. Despite first appearances, the system is analytically tractable in many cases.

Acknowledgments.

Start acknowledgments here.

REFERENCES

Blumen, W., 1978: Uniform potential vorticity flow: Part i. theory of wave interactions and two-dimensional turbulence. *J. Atmos. Sci.*, **35**, 774–783.

Carton, X., 2009: Instability of surface quasigeostrophic vortices. *J. Atmos. Sci.*, **66**, 1051–1062.

Carton, X., G. R. Flierl, X. Perrot, T. Meunier, and M. A. Sokolovskiy, 2010: Explosive instability of geostrophic vortices. part 1: baroclinic instability. *Theor. Comput. Fluid Dyn.*, **24**, 125–130.

Dritschel, D. G., 1989: On the stabilization of a two-dimensional vortex strip by adverse shear. *J. Fluid Mech.*, **206**, 193–221.

Eady, E. T., 1949: Long waves and cyclone waves. *Tellus*, **1**, 33–52.

Farrell, B. F. and P. J. Ioannou, 1996: Generalised stability theory. part i: Autonomous operators. *J. Atmos. Sci.*, **53**, 2025–2040.

Flierl, G. R., 1988: On the instability of geostrophic vortices. *J. Fluid Mech.*, **197**, 349–388.

Gradshteyn, I. S. and I. M. Ryzhic, 2000: *Table of Integrals, Series and Products*. 6th ed., AP.

Harvey, B. J. and M. H. P. Ambaum, 2010a: Instability of surface temperature filaments in strain and shear. *Quart. J. Roy. Meteor. Soc.*, in press.

Harvey, B. J. and M. H. P. Ambaum, 2010b: Perturbed rankine vortices in surface quasi-geostrophic dynamics. *Geo. and Astr. Fluid Dyn.*, in press.

Held, I. M., R. T. Pierrehumbert, S. T. Garner, and K. L. Swanson, 1995: Surface quasi-geostrophic dynamics. *J. Fluid Mech.*, **282**, 1–20.

Juckes, M., 1994: Quasigeostrophic dynamics of the tropopause. *J. Atmos. Sci.*, **51**, 2756–2768.

Juckes, M., 1995: Instability of surface and upper-tropospheric shear lines. *J. Atmos. Sci.*, **52**, 3247–3262.

Lapeyre, G. and P. Klein, 2006: Dynamics of the upper oceanic layers in terms of surface quasigeostrophy theory. *J. Phys. Ocean.*, **36**, 165–176.

Morel, Y. G. and X. J. Carton, 1994: Multipolar votices in two-dimensional incompressible flows. *J. Fluid Mech.*, **267**, 23–51.

Muraki, D. J. and C. Snyder, 2007: Vortex dipoles for surface quasigeostrophic models. *J. Atmos. Sci.*, **64**, 2961–2967.

List of Figures

5 Some example temperature profiles. Smooth curves are the C09 profiles of (30), for the α values shown, and the discontinuous profiles are the corresponding shielded Rankine vortices given by (35)-(36). 24

6 Panel (a): Normal mode growth rates scaled by S for vortices with zero integrated temperature anomaly. Wavenumbers 2–4 are indicated, the higher modes follow the pattern. The most unstable mode at each λ is emphasised by the heavy line and the dashed line represents $\max(\mathrm{F})S = 0.1292...S$ (see text). Panel (b): Scaled normal mode growth rates versus equivalent wavenumber κ_{equiv} for $\lambda = 1.7$, 1.5, 1.3 and 1.1, labelled a–d respectively. The dashed line shows the dispersion relation for a straight temperature filament. 25

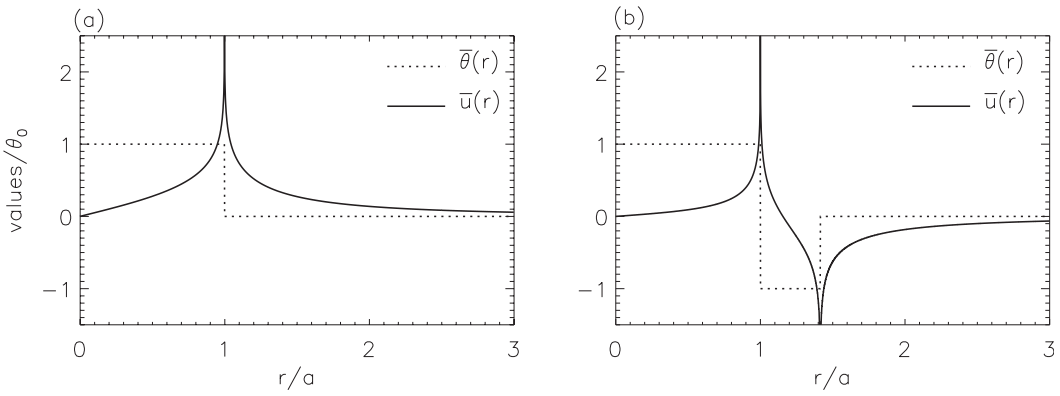

FIG. 1. Panel (a): Basic state temperature and velocity profiles for the one-step surface Rankine vortex, (1) and (2). Panel (b): Example temperature and velocity profile for a shielded surface Rankine vortex, (10), with parameter values $b = \sqrt{2}a$ and $\theta_1 = -\theta_0$.

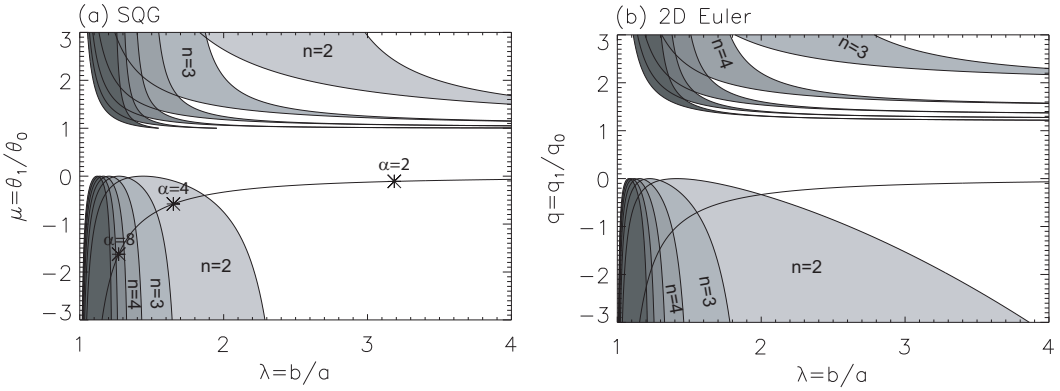

FIG. 2. Panel (a): Stability boundary in (λ, μ)-space for wavenumbers $n = 2 - 7$. The solid line indicates vortices with zero integrated temperature, see (29), and the asterisks indicate the positions of the profiles (35)-(36) for several α values. Panel (b): Stability boundary for the two-dimensional Euler problem. The solid line indicates vortices with zero integrated vorticity.

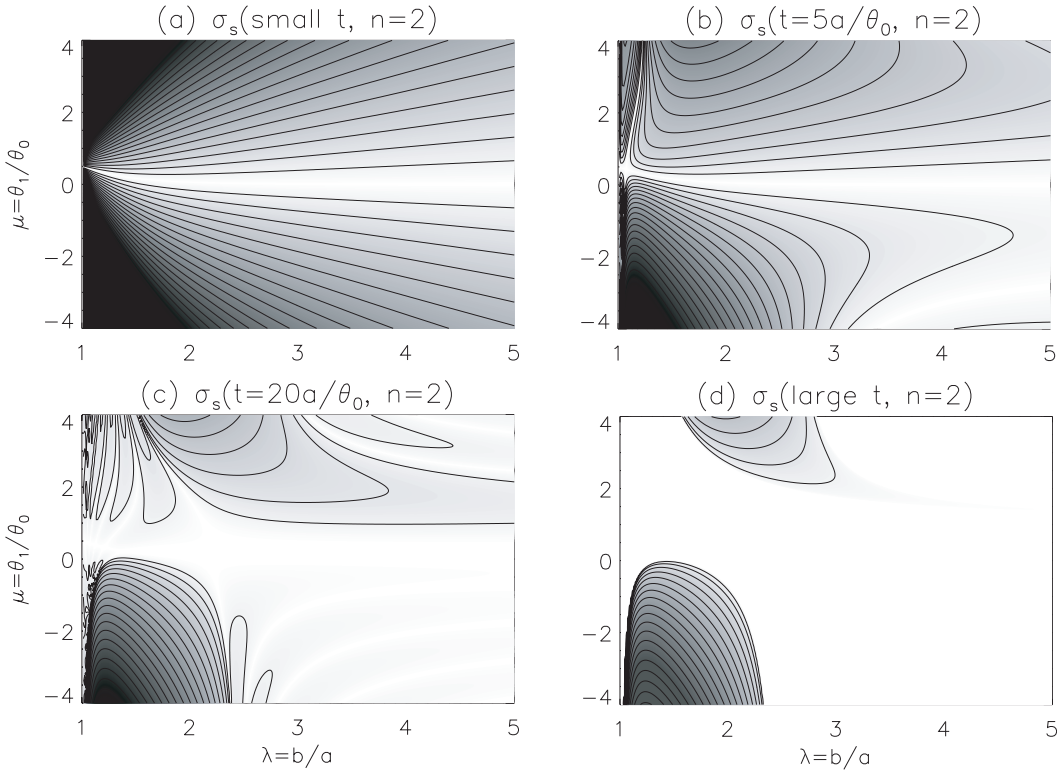

FIG. 3. Contoured values of σ_s for wavenumber $n = 2$ and t values as indicated. The small and large t plots are given by the formulae (26) and (27) respectively. The contour interval is $0.05\theta_0/a$ with dark shading indicating high values and black shading indicating values greater than θ_0/a.

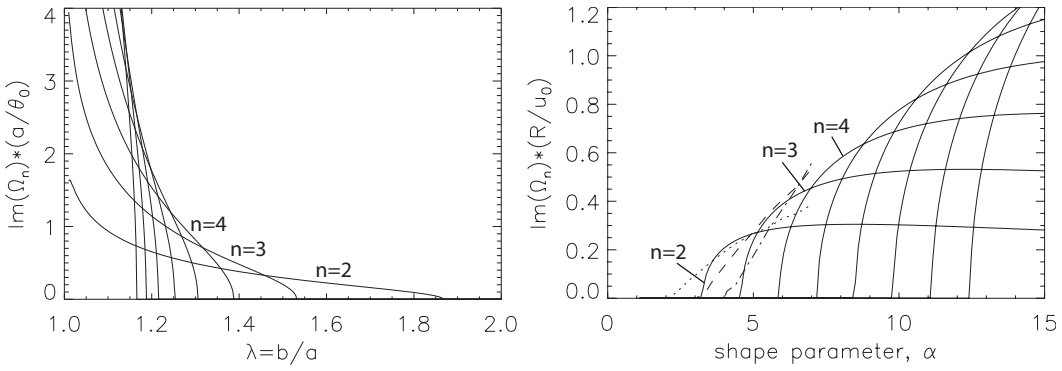

FIG. 4. Panel (a): Normal mode growth rates for completely shielded vortices as a function of λ. Panel (b) Normal mode growth rates for the parameter values (35)–(36) as a function of α. In both panels, wavenumbers 2–4 are indicated, the higher modes follow the pattern. In panel (b) the broken lines show data from C09 (see text) where dotted is $n = 2$, dashed is $n = 3$ and dot-dash is $n = 4$.

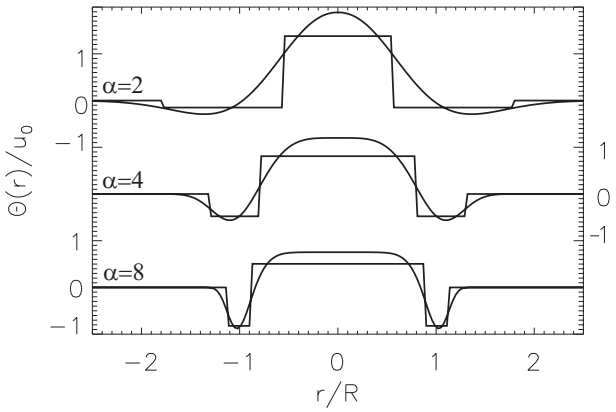

FIG. 5. Some example temperature profiles. Smooth curves are the C09 profiles of (30), for the α values shown, and the discontinuous profiles are the corresponding shielded Rankine vortices given by (35)-(36).

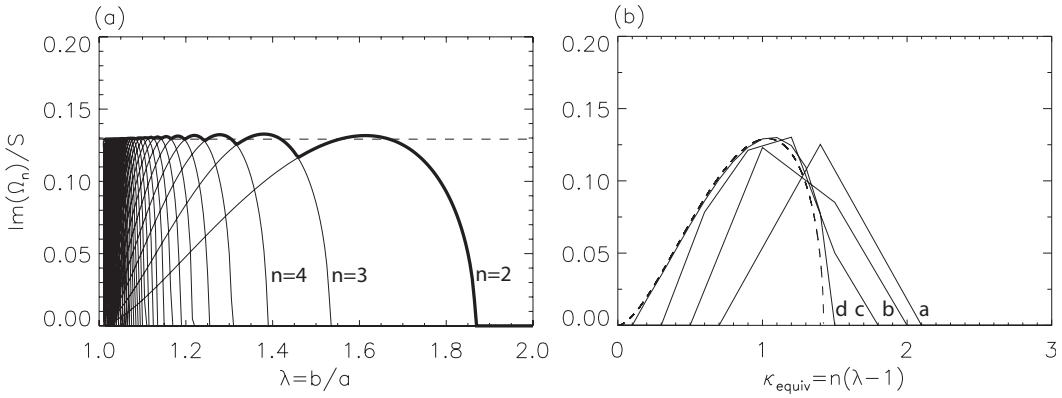

FIG. 6. Panel (a): Normal mode growth rates scaled by S for vortices with zero integrated temperature anomaly. Wavenumbers 2–4 are indicated, the higher modes follow the pattern. The most unstable mode at each λ is emphasised by the heavy line and the dashed line represents max(F)S = 0.1292...S (see text). Panel (b): Scaled normal mode growth rates versus equivalent wavenumber $\kappa_{\rm equiv}$ for λ = 1.7, 1.5, 1.3 and 1.1, labelled a–d respectively. The dashed line shows the dispersion relation for a straight temperature filament.